Article

Facile Synthesis of Bio-Template Tubular MCo₂O₄ (M = Cr, Mn, Ni) Microstructure and Its Electrochemical Performance in Aqueous Electrolyte

Deepa Guragain [1], Camila Zequine [2] , Ram K Gupta [2] and Sanjay R Mishra [1],*

[1]   Department of Physics and Materials Science, The University of Memphis, Memphis, TN 38152, USA; ddeepag13@gmail.com
[2]   Department of Chemistry, Pittsburg State University, Pittsburg, KS 66762, USA; camilazequine@hotmail.com (C.Z.); rgupta@pittstate.edu (R.K.G.)
*   Correspondence: srmishra@memphis.edu

check for updates

Abstract: In this project, we present a comparative study of the electrochemical performance for tubular MCo_2O_4 (M = Cr, Mn, Ni) microstructures prepared using cotton fiber as a bio-template. Crystal structure, surface properties, morphology, and electrochemical properties of MCo_2O_4 are characterized using X-ray diffraction (XRD), gas adsorption, scanning electron microscopy (SEM), Fourier transforms infrared spectroscopy (FTIR), cyclic voltammetry (CV), and galvanostatic charge-discharge cycling (GCD). The electrochemical performance of the electrode made up of tubular MCo_2O_4 structures was evaluated in aqueous 3M KOH electrolytes. The as-obtained templated MCo_2O_4 microstructures inherit the tubular morphology. The large-surface-area of tubular microstructures leads to a noticeable pseudocapacitive property with the excellent electrochemical performance of $NiCo_2O_4$ with specific capacitance value exceeding 407.2 F/g at 2 mV/s scan rate. In addition, a Coulombic efficiency ~100%, and excellent cycling stability with 100% capacitance retention for MCo_2O_4 was noted even after 5000 cycles. These tubular MCo_2O_4 microstructure display peak power density is exceeding 7000 W/Kg. The superior performance of the tubular MCo_2O_4 microstructure electrode is attributed to their high surface area, adequate pore volume distribution, and active carbon matrix, which allows effective redox reaction and diffusion of hydrated ions.

Keywords: bio-template; MCo_2O_4 (M = Cr, Mn, Ni); electrochemical; cyclic voltammetry; specific capacitance

1. Introduction

Supercapacitors (SCs) are the energy storage device. SCs are in high demand because of their greater power density compared to batteries and higher energy density compared to that of capacitors [1]. In the capacitor, there is no time lag during the charging process; hence it can give higher power density, and in the battery, there is low self-discharge so that it can provide higher energy density [2]. Because of this, a supercapacitor is easy to charge within a short time and able to show significant performance even after prolonged use. SCs are of three types: (i) electric double-layer capacitors (EDLCs), (ii) pseudo capacitors (PCs), and (iii) hybrid capacitors. EDLCs are based on the principle that physical adsorption takes place on the interface of a solid electrode, usually carbon-based material, and liquid electrolytes [3,4]. In PCs, surface redox reaction takes place at the electrode-electrolyte interface, which is responsible for storing electronic charges [5], where metal oxides and conducting polymer-based materials are used as active electrode materials [6,7]. EDLCs have lower specific capacitance and energy density as compared to PCs, hence, practically PCs are in higher demand.

A hybrid capacitor is a combination of both EDLCs and PCs; examples are carbon nanotubes, graphene, etc. [8,9]. They display hybrid charge–storage mechanisms and have the ability to deliver higher capacity [10].

The electrolyte ion transport in supercapacitor devices occurs through an ion-transport layer separated from the electrode. The charge storage mechanism follows at the electrode surface during the charging-discharging process [11].

Transition metal oxides (TMOs) with novel nano-architectures and rich in redox reactions are increasingly explored for their application in energy storage devices [12]. Among these, cobalt oxides are highly attractive because of their higher theoretical value for specific capacitance, i.e., 3560 F/g [13]. The nanoarchitecture of these metal-oxides is controlled by the synthesis route, which often requires complex technological strategies, including toxic organic reagents, which might make it difficult for their mass industrial application. Thus, it is highly sought to explore cost-effective facile synthesis strategies and environmentally benign techniques for preparing these electrodes. Furthermore, the ideal electrode should have a high specific surface area for better specific capacitance, controlled porosity for better rate capability as well as specific capacitance, and higher electronic conductivity to improve rate capability and power density of supercapacitor. Nowadays, the bio-templating technique has emerged as a convincing technique for the preparation of oxide supercapacitors [14–17]. Nature offers rich and diverse bio-templates [18–20] like bamboo, lotus pollen grains [21], leaf [22], sorghum straw [23], butterfly wing [24], jute fibers [25], and cotton [12]. Such bio-templates offer elaborate interior and exterior surfaces, and geometries, which make these templates attractive materials to produce multiscale hybrid and hierarchical morphologies.

Numbers of research are published on the study of transition metal oxide-based electrodes such as $MnCo_2O_4$ [5,26–28] and $NiCo_2O_4$ [29–33], Co_3O_4 [34], and $NiFe_2O_4$ [35] for their supercapacitive application. The benefit of transition metal oxides as electrode materials are innumerable, as their multiple oxidation states facilitate multiple redox reactions during electrochemical reaction vis-a-vise offers stable structure. The co-existence of two different cations provides abundant active sites to perform fast reversible faradic redox reaction on the electrode interface; as a result, higher specific capacity, and excellent rate capability are achieved [25,36]. Additionally, the types of bonds between transition metal ions and ligands are dictated by electronegativity and ionization energies [37]; with the former, the structure is dense, while with later the structure is more open. The valence state, ionic radius, electronegativity [38], and the local environment of the cations are affected by the change in Gibbs free energy and electrochemical potential of the electrode. An increase in the electrochemical potential of cathodes is observed with the increase in the number of electrons in *d* orbitals of transition metal elements. This implies a higher consumption of energy during electron transfer [39]. In mixed transition metal oxides, there is a synergetic effect between metal cations; this produces higher electrical conductivity of single metal oxide where there is low activation energy to transfer electron between metal cations and gives excellent structural stability [40,41].

Here we present a comparative study to understand the electrochemical behavior of MCo_2O_4 (M = Cr, Mn, and Ni) electrodes prepared via a facile bio-template method. The electronegativity differences among M ions viz. Cr (1.66), Mn (1.55), Ni (1.99), and Co (1.88) could have a substantial effect on the electrochemical performance of the said electrodes. The electronegativity difference determines the structure, covalent vs. ionic, and the electric potential of the electrode for the charge transfer, as discussed above. In the present study, MCo_2O_4 electrode material is prepared via the bio-template method, where the product assumes the morphology of the microstructure of bio-template and ends up with a carbon matrix. The bio-template method adapted to produce active material inherently fixed in the carbon matrix. The carbon matrix is known to enhance electrode electrochemical performance [42]. The template supported mineralization MCo_2O_4 at room temperature (RT) produces 3D-hierarchical and porous-MCo_2O_4 superstructures with tubular-like morphologies. The doped Co_3O_4 (MCo_2O_4) is explicitly explored in this study as dopant atoms or vacancies are known to affect the crystal field [43], thus modifying the electronic structure and adjusting the electrochemical potential [44].

2. Experimental

2.1. Synthesis

　　All the chemicals required for the synthsis, such as Cobalt nitrate hexahydrate; $Co(NO_3)_2.6H_2O$, Chromium nitrate hexahydrate; $Cr(NO_3)_2.6H_2O$, Manganese nitrate hexahydrate; $Mn(NO_3)_2.6H_2O$, and Nickel nitrate hexahydrate; $Ni(NO_3)_2.6H_2O$ were purchased from Sigma-Aldrich, St. Louis, Missouri, USA. The spinel MCo_2O_4 (M = Cr, Mn, Ni) was synthesized by a facile bio-template method. Quantities of 1.16 g of $Co(NO_3)_2.6H_2O$ and 0.8 gm of $Cr(NO_3)_2.6H_2O$, 0.55 g of $Co(NO_3)_2.6H_2O$ and 0.17 gm of $Mn(NO_3)_2.6H_2O$, and 0.86 g of $Co(NO_3)_2.6H_2O$ and 0.43 gm of $Ni(NO_3)_2.6H_2O$ were mixed in 15 ml of distilled water separately, and the mixture was ultra-sonicated for 10 minutes to make a homogenous solution. Then, 1.0 g of cotton was soaked in the mixture solutions for 5 minutes. The resulting soaked cotton was filtered and dried at 150 °C for 30 minutes. The dried cotton was later calcined at 520 °C for 3 hours in the air to obtain bio-templated $CrCo_2O_4$, $MnCo_2O_4$, and $NiCo2O4$ tubular microstructure.

2.2. Characterization

　　The x-ray diffraction patterns were obtained via Bruker D8 Advance X-ray diffractometer (Bruker Corporation, Madison, WI, USA) using Cu K_α radiation to check phase purity and determine the crystalline parameters of as-prepared samples. A scanning electron microscope (Phenom) at 10 keV analyzed the morphology of samples. The Brunauer–Emmett–Teller (BET) method was used to measure the specific surface area of the samples. The surface area measurement was carried out by adsorption-desorption isotherms at 77 K, (Quantachrome, Boynton Beach, FL 33426, model No. AS1MP) using nitrogen as adsorbing gas. Thermogravimetric analyses (TGA, Instrument Specialist, Inc., Twin Lakes, WI, USA), were performed in 24 to 550 °C temperature range. FTIR spectra were collected via Theromo-Fisher Scientific FTIR spectrometer (Nicolet iS10, Thermo Fisher Scientific, Waltham, MA, USA) between 450 and 1000 cm^{-1}.

　　Versastat 4–500 electrochemical workstation (Princeton Applied Research, USA) was used to perform electrochemical measurements in a standard three-electrode configuration. To prepare an electrode, slurry pastes of 80 wt % of the synthesized powder, 10 wt % of acetylene black, and 10 wt % of polyvinylidene difluoride (PVDF) were mixed in the presence of N-methyl pyrrolidinone (NMP). The thoroughly mixed paste was applied onto a nickel foam. Here, the active mass is 80% out of the total pasted mass in the electrode. The prepared electrodes were dried under vacuum at 60 °C for 10 hours. The loading mass of all samples was about 2–3 mg, measured by weighing the nickel foam before and after deposition with an analytical balance (MS105DU, Mettler Toledo, 0.01 mg of resolution). MCo_2O_4 (M = Cr, Mn, Ni) coated nickel foam was used as a working electrode, a saturated calomel electrode (SCE) as a reference electrode, and a platinum wire as a counter electrode. The electrochemical performance of the electrodes was evaluated at RT in 3M KOH electrolyte via cyclic voltammetry and galvanostatic charge-discharge techniques measurements.

3. Results and Discussion

　　Figure 1a shows the XRD patterns of the bio-templated $CrCo_2O_4$, $MnCo_2O_4$, and $NiCo_2O_4$ microstructure. The XRD patterns match with the face-centered cubic phase of $CrCo_2O_4$, $MnCo_2O_4$, and $NiCo_2O_4$ (International Centre for Diffraction Data (ICDD) #02-0770). The main peaks at 30.9°, 36.4°, 44.3°, 58.6°, and 64.3° for $CrCo_2O_4$, 31.1°, 36.7°, 44.7°, 59.2°, and 65.9° for $MnCo_2O_4$, and 31.3°, 36.8°, 44.8°, 59.4°, and 65.2° for $NiCo_2O_4$ can be assigned to the (220), (311), (400), (511) and (440) reflections of $CrCo_2O_4$, $MnCo_2O_4$, and $NiCo_2O_4$ respectively [45,46]. The pattern of $NiCo_2O_4$ shows a peak at 43.2°, which indicates the formation of NiO cubic phase as also confirmed by TOPAS fitting. The lattice constants obtained using *d*-spacing for the sample are $a = b = c = 0.816$ nm, 0.808 nm, 0.807 nm, and for $CrCo_2O_4$, $MnCo_2O_4$, and $NiCo_2O_4$, respectively. The crystallite size of $CrCo_2O_4$, $MnCo_2O_4$, and $NiCo_2O_4$ as calculated using Scherrer's formula [47] is around 10.57 nm, 14.65 nm, and 19.97 nm for

$CrCo_2O_4$, $MnCo_2O_4$, and $NiCo_2O_4$, respectively (Table 1). FTIR spectrum, Figure 1b, further identifies the structure of the bio-templated MCo_2O_4. The FTIR spectrum displays two distinct bands at 515.7 (v_1) and 637 (v_2) cm^{-1}, which arise from the stretching vibrations of the metal-oxygen bonds [48–50]. The v_1 band is characteristic of M-O (M = Cr, Mn, Ni) vibrations in octahedral coordination, and the v_2 band is attributable to M-O (M - Co) bond vibration in tetrahedral coordination. These frequency bands are the signature vibrational bands for the spinel lattice [51]. Hence FTIR spectrum at 519.1, 519.02, and 519.08 cm^{-1} indicate stretching vibration of Co^{3+}-O^{2-} in the octahedral sites, and at 638.6, 639.9, and 641.3 cm^{-1} indicate vibration of Cr^{3+}-O^-, Mn^{2+}-O^{2-}, and Ni^{2+}-O^- at tetrahedral sites for $CrCo_2O_4$, $MnCo_2O_4$, and $NiCo_2O_4$, respectively [52]. The presence of vibration bands confirms the development of pure phase spinal $CrCo_2O_4$, $MnCo_2O_4$, and $NiCo_2O_4$ nanostructures.

Table 1. Crystallite size and physical properties of MCo_2O_4 (M = Cr, Mn, Ni) determined using XRD, the Barrette–Joyner–Halenda (BJH) method, and Brunauer–Emmett–Teller (BET) surface area analyzer.

Sample	BET Surface Area(m^2/g)	BJH Surface Area (m^2/g)	BJH Avg. Pore Radius (nm)	BJH Avg. Pore Volume (cc/g)	Crystallite Size (nm)
$CrCo_2O_4$	34.4	46.9	1.135	0.106	10.57
$MnCo_2O_4$	32.2	47.7	0.839	0.071	14.65
$NiCo_2O_4$	18.9	31.8	1.129	0.039	19.97
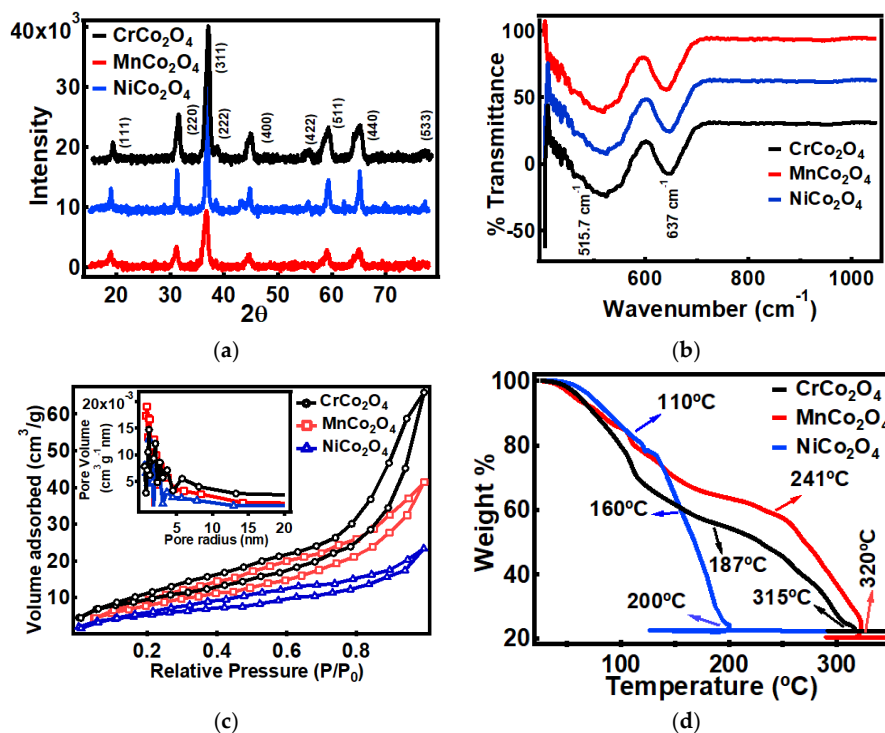
Figure 1. (**a**) x-ray diffraction pattern, (**b**) FTIR, (**c**) adsorption-desorption curve and inset pore volume distribution, and (**d**) thermogravimetric curve of tubular MCo_2O_4 (M = Cr, Mn, Ni) structures.

Figure 1c shows the BET specific surface area of tubular MCo_2O_4 microstructures. The specific surface area was determined from N_2 adsorption-desorption isotherms obtained at 77 K between relative pressure P/P_o~0.029 to 0.99, and the Barrette–Joyner–Halenda (BJH) method was used for measuring corresponding pore sized distributions. The type IV isotherm hysteresis loops [53] suggest the existence of mesopores in the samples. The BET specific surface area of biomorphic $CrCo_2O_4$, $MnCo_2O_4$, and $NiCo_2O_4$ are 34.4 m^2/g, 32.2 m^2/g, and 18.9 m^2/g, respectively. Figure 1c inset shows the pore size distribution. Inset curves indicate having a more favorable condition for the fast ion transport phenomenon within the electrode surface [54–57], which is confirmed by the presence of a significant number of pores distribution at around 0.4 nm to 4.3 nm with the highest pore volume.

Additionally, the large BET surface area of tubular MCo_2O_4 superstructures can provide plenty of superficial electrochemical active sites to participate in the Faradaic redox reactions.

The thermogravimetric analysis was conducted on the infiltrated samples (cotton dipped in a mixture of chemical solution and filtered it) to understand the temperature dependence mechanism of the formation of biomorphic MCo_2O_4. Figure 1d shows the TGA plots of MCo_2O_4 measured in the temperature range of 24 to 550 °C. The formation of MCo_2O_4 from the nitrate salts results in three steps. The weight loss at around 110 °C for all three MCo_2O_4 is due to water desorption, the second weight loss up to 187 °C for $CrCo_2O_4$, 241 °C for $MnCo_2O_4$, and 160 °C for $NiCo_2O_4$ is due to burning of cotton and start of decomposition of $Co(NO_3)_2 \cdot 6H_2O$ and $Cr(NO_3)_2 \cdot 6H_2O$, $Co(NO_3)_2 \cdot 6H_2O$ and $Mn(NO_3)_2 \cdot 6H_2O$, $Co(NO_3)_2 \cdot 6H_2O$ and $Ni(NO_3)_2 \cdot 6H_2O$ respectively, there was no weight loss at beyond 315, 320, and 200 °C which signifies the completion of the formation of $CrCo_2O_4$, $MnCo_2O_4$, and $NiCo_2O_4$. Upon immersing fiber into the precursor solution, the water and $Cr(NO_3)_2 \cdot 6H_2O$, $Mn(NO_3)_2 \cdot 6H_2O$, $Co(NO_3)_2 \cdot 6H_2O$ and $Ni(NO_3)_2 \cdot 6H_2O$ molecules were absorbed onto the hydroxyl-group-rich cotton fiber substrate. With the heat treatment above 520 °C, nitrate salts decomposed in the form $CrCo_2O_4$, $MnCo_2O_4$, and $NiCo_2O_4$ as follow [58],

$$2Co(NO_3)_2 \cdot 6H_2O + Cr(NO_3)_2 \cdot 6H_2O \rightarrow CrCo_2O_4 + 2O_2 + 6NO_2 + 18H_2O \qquad (1)$$

$$2Co(NO_3)_2 \cdot 6H_2O + Mn(NO_3)_2 \cdot 6H_2O \rightarrow MnCo_2O_4 + 2O_2 + 6NO_2 + 18H_2O \qquad (2)$$

$$2Co(NO_3)_2 \cdot 6H_2O + Ni(NO_3)_2 \cdot 6H_2O \rightarrow NiCo_2O_4 + 2O_2 + 6NO_2 + 18H_2O \qquad (3)$$

With the increase in calcination temperature, the removal of organic substance was achieved where the remaining few portions of the organic substance change into carbon.

FE-SEM in Figure 2a–d displays tubular morphology of the cotton fibers, samples $CrCo_2O_4$, $MnCo_2O_4$, and $NiCo_2O_4$, respectively, which resembles a biomorphic structure. Figure 3a–c shows SEM images obtained using elemental mapping at chromium, manganese, and nickel energy peaks and shows that the tubular structure is well decorated with the $CrCo_2O_4$, $MnCo_2O_4$, and $NiCo_2O_4$ nanoparticles. Table 2 gives the elemental composition and element distribution, which is obtained via EDX (energy dispersive x-ray spectroscopy).
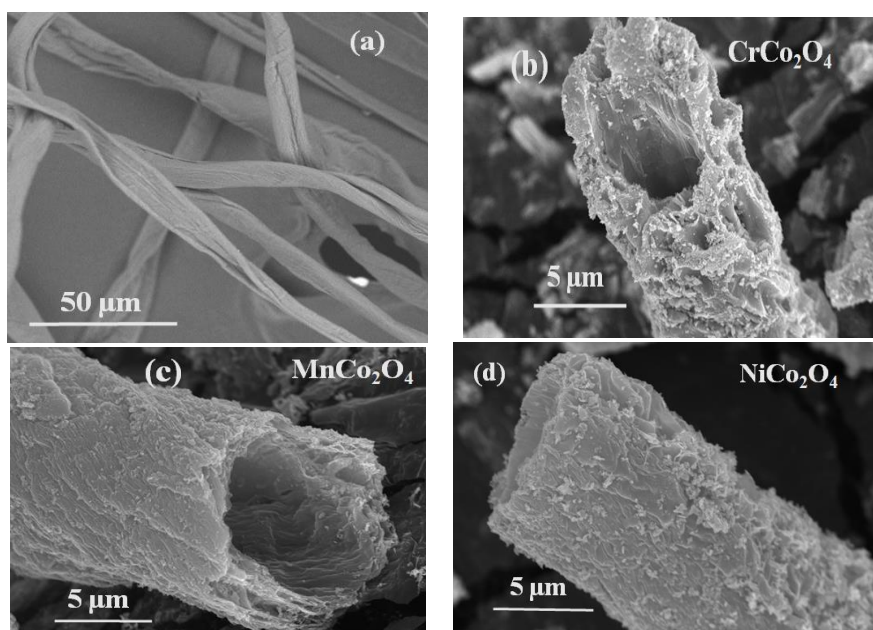
Figure 2. SEM images of (**a**) cotton fiber, (**b**), (**c**), and (**d**) bio-templated tubular MCo_2O_4 (M = Cr, Mn, Ni) structures.

(a)

(b)

(c)
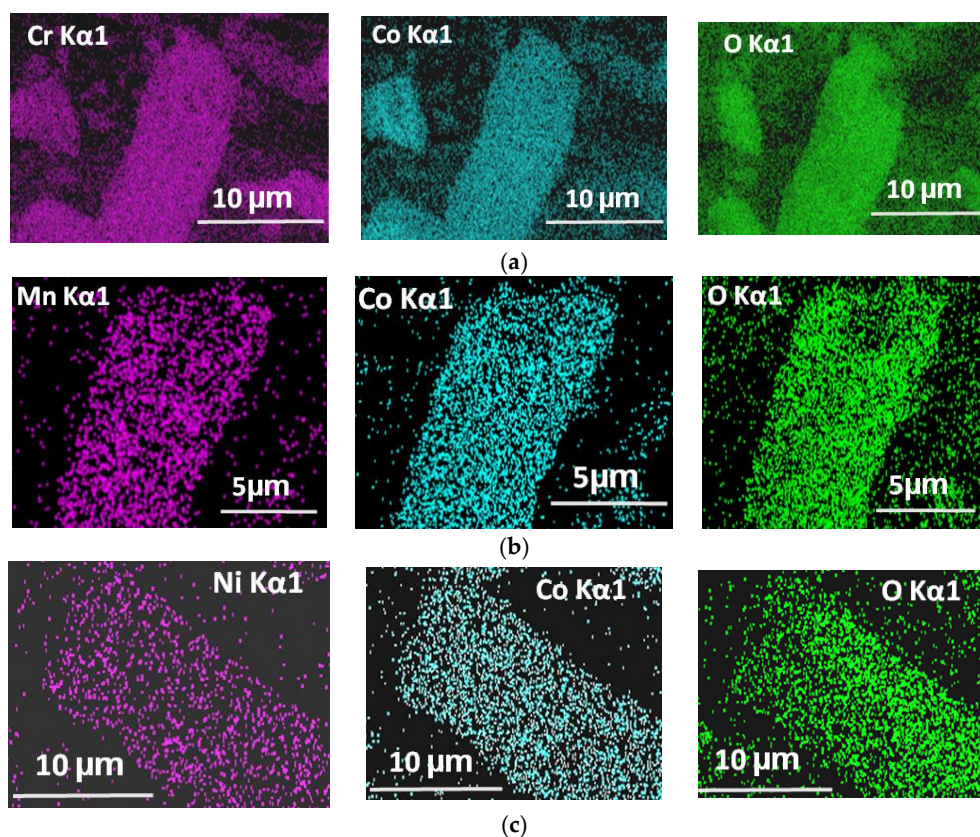
Figure 3. (**a**), (**b**), and (**c**) shows EDX mapping of tubular MCo_2O_4 (M = Cr, Mn, Ni) structures, respectively.
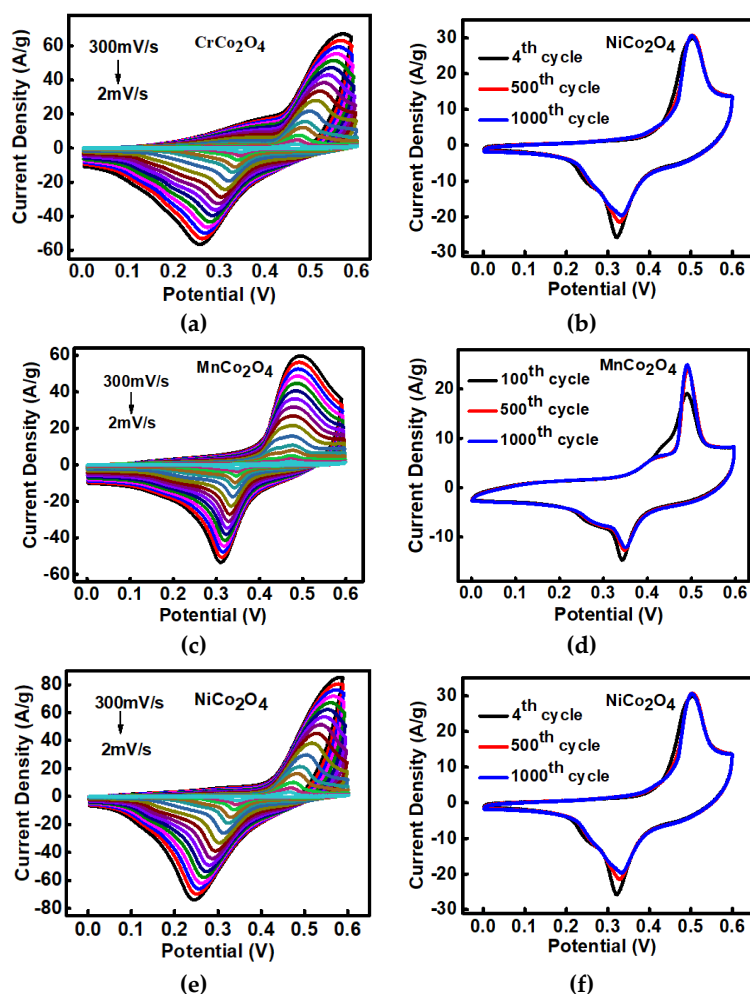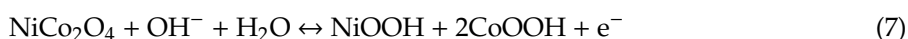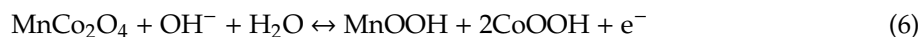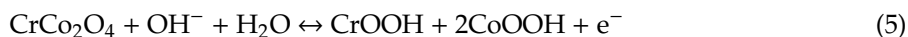
Table 2. Elemental composition in wt % for MCo_2O_4 (M = Cr, Mn, Ni) obtained using energy dispersive X-Ray analysis (EDX). The elemental composition is approximately determined using EDX. Ideally, EDX can prove which elements are abundant in the particles, but not obtain the exact chemical composition.

	Co	C	O	Cr	Mn	Ni
$CrCo_2O_4$	19.5	49.4	23.2	7.8		
$MnCo_2O_4$	33.1	34.6	23.5		8.8	
$NiCo_2O_4$	27.2	42.4	19.3			11.1

The type of electrolytes and their molar concentration play a vital role in determining the electrochemical behavior of oxide electrodes [59–61]. Therefore, many aqueous electrolytes such as sulfates K_2SO_4, H_2SO_4, KNO_3, Na_2SO_4, hydroxyl KOH, NaOH, LiOH, and chlorides KCl, NaCl have been explored to be used in supercapacitors [62–66]. The ultimate performance of the electrode is based on the properties of the electrode material and the intercalation efficiency of the cations [51]. Since KOH electrolyte provides lower electrochemical series resistance with better conductivity as compared to other electrolytes [67], KOH is chosen as an electrolyte in this study for the electrochemical measurement.

Cyclic voltammetry and charge-discharge curves were measured to investigate the electrochemical behavior of MCo_2O_4 nanoparticles. Figure 4 displays the CV curves for tubular MCo_2O_4 electrodes measured in the 3M KOH electrolyte. Figure 4a,c, and Figure 4e shows the CV curves measured in the voltage window of 0.0 to 0.6 V and measured at different scan rate from 2 to 300 mV/s. A pair of redox peaks associated with the redox reactions involved in the alkaline electrolyte during the charging and discharging process was observed in all CV plots. The CV curve is asymmetric, which indicates a quasi-reversible redox reaction [68], the anodic and cathodic peak separation are 0.121 V, 0.124 V, and 0.123 V at 2 mV/s and 0.310 V, 0.186 V, and 0.333 V at 300 mV/s for $CrCo_2O_4$, $MnCo_2O_4$ and $NiCo_2O_4$ respectively. The presence of anodic and cathodic peaks, indicating the usefulness of

the materials as a pseudocapacitor. Typical pseudo-capacitance behavior of MCo_2O_4 nanostructures arises from the reversible surface or near-surface Faradic reactions for charge storage. The reversible redox reaction involved in the charge-discharge process for MCo_2O_4 can be described as follows by Equations (5)–(7) [69–71].

$$MO + OH^- \leftrightarrow MOOH + e^- \tag{4}$$

$$CrCo_2O_4 + OH^- + H_2O \leftrightarrow CrOOH + 2CoOOH + e^- \tag{5}$$

$$MnCo_2O_4 + OH^- + H_2O \leftrightarrow MnOOH + 2CoOOH + e^- \tag{6}$$

$$NiCo_2O_4 + OH^- + H_2O \leftrightarrow NiOOH + 2CoOOH + e^- \tag{7}$$

Figure 4. (**a,c,e**) show cyclic voltammetry curves of tubular MCo_2O_4 (M = Cr, Mn, Ni) electrode obtained in the scan range of 5 mV/s to 300 mV/s measured in 3M KOH electrolyte. (**b,d,f**) show cyclic stability curves measured up to 1000 cycles in 3M KOH electrolyte at scan rate of 40 mV/s.

Pseudocapacitive characteristics of electrodes are indicated by a non-rectangular form of CV curves. Within the potential range from 0 to 0.6 V, a pair of reversible redox peaks can be observed. With the increase in the scan rate, a small positive shift of the oxidation peak potential and a negative shift of the reduction peak potential was observed, which can be primarily attributed to the influence of the increasing electrochemical polarization as the scan rate scales up. Pairs of reversible redox curve are indicative of pseudocapacitive behavior of the material with redox peaks attributed to M(II)/M(III) redox process [72]. The redox potentials and shape of the CV curves are comparable to those reported

for CrCo$_2$O$_4$, MnCo$_2$O$_4$, and NiCo$_2$O$_4$ electrodes [24,73–76], suggesting that the measured capacitance mainly arises from the redox mechanism.

Figure 5a shows the specific capacitance, C_{sp}, as a function of the voltage scan rate of the tubular MCo$_2$O$_4$ electrode. The specific capacitance, C_{sp}, was calculated from the CV plots using the following Equation (8) [77].

$$C_{sp} = \frac{\int_{V1}^{V2} i * V * dV}{m * v * (V2 - V1)} \tag{8}$$

where V_1 and V_2 stand for the working potential limits, i stands for the current, m stands for the mass of the electroactive materials, and v is the scan rate in mV/s.
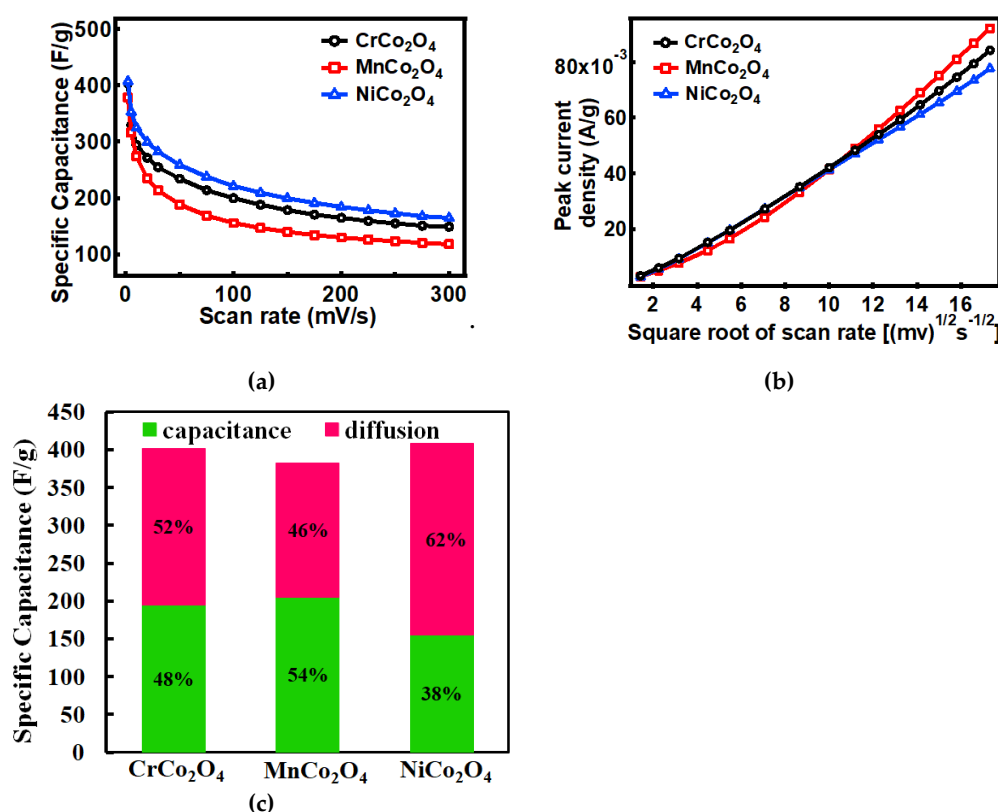
Figure 5. (**a**) Specific capacitance vs. scan rate, (**b**) and peak current vs. (scan rate)$^{1/2}$, and (**c**) diffusion and capacitive contribution to the specific capacitance.

It is evident for this figure that the electrode displays higher C_{sp} up to 407.2 F/g for NiCo$_2$O$_4$ in 3M KOH electrolyte at 2 mV/s, which is higher than the value that is observed for either CrCo$_2$O$_4$ (C_{sp} ~ 403.2 F/g) or MnCo$_2$O$_4$ (C_{sp} ~ 378.1 F/g) electrode, value are given in Table 3. The specific capacitance for higher scan rates (>50 mV/s) remains practically constant because of limited ion movement only at the surface of the electrode material. Hence EDLC becomes a dominant mechanism at higher scan rates. At lower scan rates (<5 mV/s), the majority of active surface are utilized by the ions for charge storage, and hence resulting in the higher specific capacitance. The CV cyclic stability of the electrode was tested for 1000 cycles. Figure 4b,d, and Figure 4f show no significant differences in the CV curves after the 100th, 500th, and 1000th cycle of repetition. The CV curves clearly show that the current response is proportionally increased with the scan rate, indicating an excellent capacitive behavior of the electrode materials. This can be ascribed to facile ion diffusion and large specific surface area of the electrode materials. Furthermore, there is almost no relation between the shape of CV curves and scan rates, which can be associated with the electron conduction and improved mass transportation of electrode material [78].

Table 3. Data of specific capacitance, energy density, and power density for MCo_2O_4 (M = Cr, Mn, Ni) obtained from cyclic voltammetry and charge-discharge curves.

	$CrCo_2O_4$	$MnCo_2O_4$	$NiCo_2O_4$
Specific Capacitance at 2mv/s	403.2 F/g	378.1 F/g	407.2 F/g
Specific Capacitance at 1A/g	231 F/g	161 F/g	190 F/g
Energy density	11.1 Wh/Kg	7.8 Wh/Kg	9.3 Wh/Kg
Power density	7287.34 W/Kg	7195.33 W/Kg	7186.12 W/Kg

The total stored charge has a contribution from three components; first is the Faradaic contribution coming from the insertion process of electrolyte ions, second is the faradaic contribution from the charge-transfer process with surface atoms, and third is pseudocapacitance and nonfaradic contribution from the double layer effect [79]. Both pseudocapacitance and double-layer charging are substantial, due to their higher surface area of nanoparticles. The capacitive effects are characterized by analyzing the cyclic voltammetry data at various scan rates according to [80,81],

$$i = av^b \qquad (9)$$

where *i, v, a* and *b*, are peak current (A), voltage scan rate (mV/s), and fitting parameters, respectively. The charge storage mechanism is defined based on the value of the constant *b*, where *b* = 1 defines capacitive or *b* = 0.5 defines diffusion-limited charge storage mechanism. Fitting the peak current, *i*, vs. square root of the scan rate, SQRT (scan rate), $v^{-1/2}$, curves, Figure 5b, with Equation (6), gives *b* values of ~ 0.646, 0.711, and 0.648 for $CrCo_2O_4$, $MnCo_2O_4$, and $NiCo_2O_4$, respectively. This obtained *b* value for our sample MCo_2O_4 (M = Cr, Mn, Ni) indicates the diffusive nature of the charge storage mechanism is prominent for $NiCo_2O_4$ as compared to the other two.

Usually, the contribution to the current response at fixed potential comes from surface capacitive effects and diffusion-controlled insertion processes [82,83]. These contributions to the specific capacitance could be separated using the following Equation (10):

$$C_{sp} = k_1 + k_2\, v^{-1/2} \qquad (10)$$

For which k_1 and k_2 can be determined from the C_{sp} *vs.* $v^{-1/2}$ linear plot with slope k_2 and intercept k_1. k_1 and k_2 are fractions of diffusion and capacitive contribution to the net specific capacitance at a given voltage rate. The C_{sp} was plotted against the slow scan rate up to 20 mV/s, and a regression fit was performed using Equation (10). The obtained k_1 and k_2 values were used to determine the fractional contribution to the net specific capacitance. Figure 5c shows capacitive and diffusive fractional contributions to net specific capacitance for a slow scan rate of up to 20 mV/s. By comparing the lower green area with the total capacitance, we find that capacitive effects contribute by 48%, 54%, and 38% of the total specific capacitance for $CrCo_2O_4$, $MnCo_2O_4$, and $NiCo_2O_4$, respectively.

Figure 6a,c, and Figure 6e show the galvanostatic charge-discharge (GCD) plots measured in the voltage window of 0.0 to 0.6 V at different current densities between 0.75 A/g to 30 A/g in 3M KOH. From the observed non-linearity between the potential and time, it is confirmed that the capacitance of the studied materials is not constant over the studied potential ranges. The specific capacitance of electrodes was calculated using the following Equation (11):

$$C_{sp} = \frac{I * t}{m * \Delta V} \qquad (11)$$

where C_{sp}, *I*, ΔV, *m, and t* are the specific capacitance (F/g), charge-discharge current (A), the potential range (V), and the mass of the electroactive materials, and the discharging time (s), respectively. The GCD curves with a plateau, usually displayed by oxide electrodes, show pseudocapacitive behavior of electrode with respect to their discharging time for all electrolytes. This typical GCD behavior could arise from the electrochemical adsorption-desorption of OH⁻ electrolyte and/or a redox reaction at the interface of electrode/electrolyte [84,85]. It is observed that the discharging time

in biomorphic MCo_2O_4 is longer for $CrCo_2O_4$ in the KOH electrolyte. The specific capacitances of biomorphic $CrCo_2O_4$, $MnCo_2O_4$, and $NiCo_2O_4$ at 1 A/g are 231 F/g, 161 F/g, and 190 F/g in 3M KOH electrolytes, respectively are shown in Table 3. Figure 7a shows the dependence of current density on the specific capacitance of the electrode material. Usually, insufficient Faradic redox reaction is achieved at the high discharge current densities. This leads to increased potential drop due to the resistance of tubular $MoCo_2O_4$ electrode resulting in an observed decrease in capacitance with the increased discharge current density. This implies ion penetration is feasible at lower current densities where ions have access to the inner structure, and thus all active area of the electrode. However, at higher current densities, the effective use of the material is limited to only the outer surface of the electrode. The specific capacitance of MCo_2O_4 electrodes in this study is compared with the literature values at current density 1 A/g, 2 A/g, and 5 A/g and are listed in Table 4. It is evident from Table 4 that electrochemical performance of bio-templated MCo_2O_4 comparable and, in some cases, outperformed electrodes prepared via other techniques.
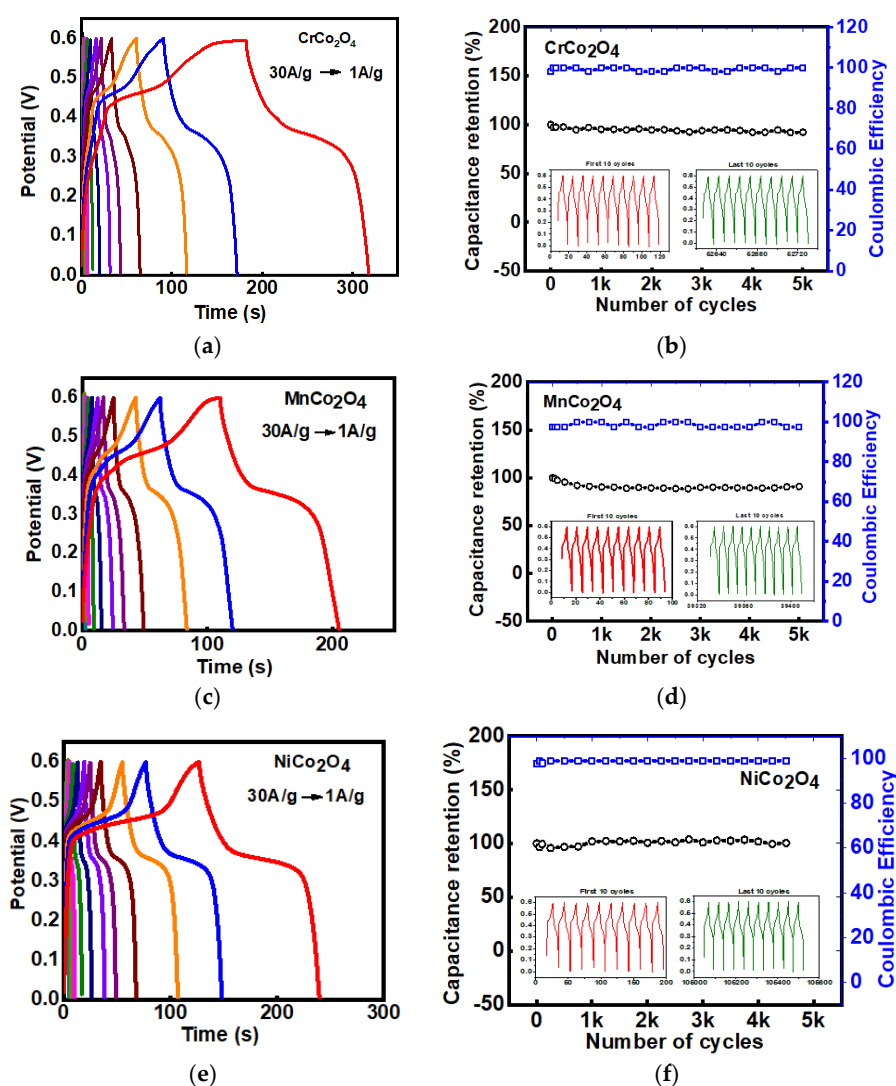
Figure 6. (**a,c,e**) show charge-discharge (CD) curves of tubular MCo_2O_4 (M = Cr, Mn, Ni) electrode measured in the current density window of 1 to 30 A/g in 3M KOH electrolyte, where red color CD curve is for 1A/g, blue color CD curve is for 1.5A/g, orange color CD curve is for 2A/g and continuously time is decreasing with increasing current density. (**b,d,f**) show cyclic stability (black color) and coulombic efficiency (blue color) tested at 10 A/g current density for 5000 cycles in 3M KOH electrolytes of MCo_2O_4 (M = Cr, Mn, Ni).
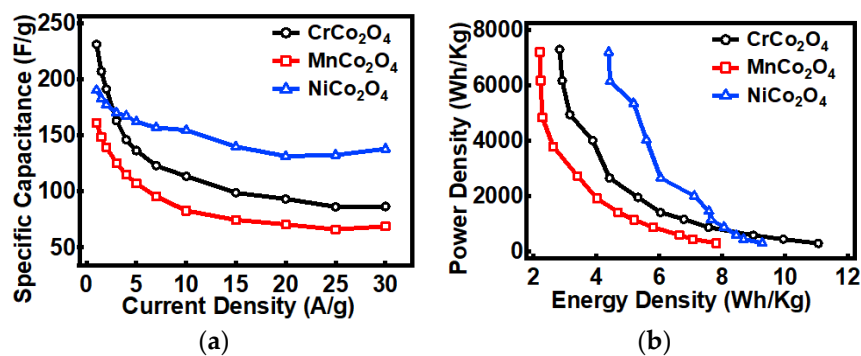
Figure 7. (**a**) Comparison of specific capacitance as a function of current density and (**b**) Ragone plot of power density vs. energy density.

Table 4. Comparison of electrochemical performance of MCo_2O_4 (M = Cr, Mn, Ni) as available from the literature.

Electrode Material	Electrolyte	Specific Capacitance	Energy Density	Power Density	Cyclic Performance (retention)	Ref.
$MnCo_2O_4$ nanofiber		108 F/g at 10 A/g	54 Wh/Kg	9851 W/Kg	85 % after 3000 cycles	[5]
Nanorods $MnCo_2O_4$	1M KOH	349.8 F/g at 1 A/g	35.4 Wh/Kg	225 W/Kg	92.7% after 50 cycles	[86]
Nanoneedles $MnCo_2O_4$	6M KOH	1535 F/g at 1 A/g	35.4 Wh/Kg	225 W/Kg	94.3% after 12000 cycles	[87]
Nanorods $MnCo_2O_4$	2M KOH	845.6 F/g at 1 A/g	35.4 Wh/Kg	225 W/Kg	90.2% after 2000 cycles	[24]
Nanorods $MnCo_2O_4$	1M KOH	308.3 F/g at 1 A/g	55.5 Wh/Kg	5400 W/Kg	88.76% after 2000 cycles	[88]
$MnCo_2O_4$ nanowires @MnO_2	-	2262 F/g at 1 A/g	85.7 Wh/Kg	800 W/Kg	-	[89]
Nanorods $MnCo_2O_4$		718 F/g at 0.5 A/g	-	-	84 % after 1000 cycles	[90]
$NiCo_2O_4$ nanorods	2M KOH	565 F/g at 1 A/g	-	-	77.6% after 1000 cycles	[69]
RGO decorated nanorods bundle $NiCo_2O_4$	6M KOH	1278F/g at 1 A/g	-	-	95% after 1000 cycles	[84]
Nanorods assemble $NiCo_2O_4$	2M KOH	764 F/g at 2 A/g	-	-	101.7% after 1500 cycles	[91]
Nanorods $NiCo_2O_4$	2M KOH	823 F/g at 0.823 A/g	28.51 Wh/Kg	-	101.7% after 1500 cycles	[2]
GO/ Nanorods $NiCo_2O_4$	1M KOH	709.7 F/g at 1 A/g	28 Wh/Kg	8000 W/Kg	94.3% after 5000 cycles	[92]
Nanorods $NiCo_2O_4$	2M KOH	600 F/g at 5 A/g	-	-	80% after 1500 cycles	[70]
Nanorods $NiCo_2O_4$ @PANI	1M H_2So_4	901 F/g at 5 A/g	-	-	91% after 3000 cycles	[93]
Templated $CrCo_2O_4$, $MnCo_2O_4$, and $NiCo_2O_4$ microstructure	3M KOH	403.4, 378, and 407.2 F/g at 2mV/s and 231, 161, and 190 F/g at 1 A/g, respectively	11.1, 7.8, and 9.3 Wh/kg, respectively	7287.3, 7195.3, and 7186.1 W/Kg, respectively	92% after 5000 cycles 91% after 5000 cycles and 100% after 5000 cycles, respectively.	[This work]

Estimation of the electrochemical utilization of the active materials ($CrCo_2O_4$, $MnCo_2O_4$, and $NiCo_2O_4$ electrode), was evaluated from the fraction of cobalt sites, z. The fraction, z, can be evaluated using Faraday's law as following [94]:

$$z = C_{sp}\ MW\ \Delta V/F \tag{12}$$

where C_{sp}, *MW*, ΔV *and F* is the specific capacitance value, the molecular weight, the applied potential window, and the Faraday's constant, respectively. The z value of 1 indicates the complete involvement of electroactive material. i.e., all active metal sites participating in the redox process. The molecular weight of Co (84.03 g/mol) and Cr (51.996 g/mol) in $CrCo_2O_4$, Co (84.03 g/mol) and Mn (54.93 g/mol) in $MnCo_2O_4$, and Co (84.03 g/mol) and Ni (58.69 g/mol) in $NiCo_2O_4$ the specific capacitance at a current density of 1 A/g (Csp~ 231 F/g, 161 F/g, and 190 F/g) for $CrCo_2O_4$, $MnCo_2O_4$, and $NiCo_2O_4$, Figure 5b, and a potential window of 0.6 V gives a z value of 0.195, 0.139, and 0.169 respectively. In other words, ~20%, 14%, and 17% of the total active material Cr, Mn, and Ni atoms participate in the redox reaction for the charge storage. The observed low value of z suggests that the charge storage in tubular MCo_2O_4 structure via a redox reaction process occurs mainly at the surface with little bulk interaction due to diffusion of OH^- ions into the material. It could be concluded that the charge storage due to the redox process in MCo_2O_4 mostly occurs only at the redox sites predominantly located on the surface of the particles [71].

Cyclic stability tests were performed to evaluate the practical performance of electrodes as a supercapacitor. The stability test of electrode materials was assessed via galvanostatic CD measurement for 5000 cycles for a current density of 10 A g^{-1} in 3M KOH and is shown in Figure 6b,d, and Figure 6f. The Coulombic efficiency (η) of the devices was calculated from its charging (T_c) and the discharging (T_d) times from GCD curves following the relation, $\eta = T_d/T_c \times 100$, and is plotted in Figure 6b,d,f as a function of cyclic time. The initial η of the device was ~100%, which remained practically the same even after 5000 cycles. For the practical applications, the study of cycling performance for electroactive material is very significant parameter. The percentage retention in specific capacitance was calculated using,

$$\text{\% retention in specific capacitance} = (C_\#/C_1)\times100 \tag{13}$$

where $C_\#$ and C_1 are specific capacitance at various cycles and the 1st cycle, respectively. The specific capacitance of the electrode is reduced by 7.68% in $CrCo_2O_4$, reduced by 9.12% in $MnCo_2O_4$, and increased by 0.48% in $NiCo_2O_4$.

Figure 5h shows the Ragone plots of as-synthesized MCo_2O_4 electrodes. The energy densities (E) and power densities (P) of the electrochemical cells are calculated using the following equations [95]:

$$E = (1/2)CV^2 \tag{14}$$

$$P = E/t \tag{15}$$

where *C*, *V*, and *t* are the specific capacitance that depends on the mass of the electrodes, the operating voltage of the cell, and discharge time in seconds, respectively. The essential point for high-performance supercapacitors is to obtain a high energy density and meanwhile providing an outstanding power density. It is observed from Figure 7b that the tubular $CrCo_2O_4$, $MnCo_2O_4$, and $NiCo_2O_4$ electrode display superior performance over energy density up to 11.1 Wh/kg, 7.8 Wh/kg, and 9.3 Wh/kg with a peak power density up to 7287.34 W/kg, 7195.33 W/kg, and 7186.12 W/kg, respectively are given in Table 3. As supercapacitor is expected to provide higher power and energy density at the same time, hence $NiCo_2O_4$ displays an overall better energy density of 9.3 Wh/kg and a power density of 7186.12 W/kg as compared to $MnCo_2O_4$ and $CrCo_2O_4$.

Ideally, to develop a higher energy density battery with a given anode, a cathode with high electrochemical interaction potential is desired. This is because the energy density of the device equals the product of the working voltage, which is obtained from the electrochemical potentials different between the cathode and anode and specific capacity of the electrode materials [63]. On the other hand, the theoretical capacity of electrode materials depend on the number of reactive electrons (*n*) and molar weight (*M*) of the materials and is expressed as Equation (16) [96],

$$C_t = n*F/3.6*M \tag{16}$$

Here, *F* is the Faraday constant, *n* is the number of reactive electrons, and *M* is the molar weight of materials. Theoretically, the equation predicts that an electrode material having a smaller molecular weight can produce a higher capacity. The molecular weight of $CrCo_2O_4$, $MnCo_2O_4$, and $NiCo_2O_4$ is ~ 233.86, 236.80, and 240.55 g/mol, respectively. Thus, in line with the Equation (11), at low current density, among three electrodes studied, the $CrCo_2O_4$ displays higher specific capacitance. However, overall superior performance in terms of energy and power density was displayed by the $NiCo_2O_4$ electrode. $NiCo_2O_4$ is known to possess rich electroactive sites, narrow pore size, and higher electrical conductivity (at least two magnitudes higher) than that of Co_3O_4 and NiO, which could be the reason for the observed overall better performance of $NiCo_2O_4$ [97,98].

4. Conclusions

In conclusion, biomorphic tubular $CrCo_2O_4$, $MnCo_2O_4$, and $NiCo_2O_4$ nanostructures were prepared using cotton by a cost-effective and straightforward bio-template method. The synthesized tubular MCo_2O_4 display excellent crystallinity, phase purity and display desirable electrochemical properties, which indicate a good chance for the fabrication of high-performance supercapacitor devices. Electrodes constructed using the tubular MCo_2O_4 demonstrate high specific capacitance, cyclic stability, power, and energy density when evaluated in 3M KOH electrolyte. The study suggests that it is imperative to account for the nature of the electroactive sites and the conductivity of materials when choosing materials from the series of transition metal oxide as the electrode for the supercapacitor application. Furthermore, the superior electrochemical performance of tubular MCo_2O_4 microstructure owes to the presence of conducting a carbonaceous structure. The highly porous carbonaceous structure can allow electrolyte access throughout the electrode structure. Thus, it produces a large surface area for ion transfer between the electrolyte and the active materials, which leads to achieving ultrafast storage and release of energy.

References

1. Suktha, P.; Chiochan, P.; Iamprasertkun, P.; Wutthiprom, J.; Phattharasupakun, N.; Suksomboon, M.; Kaewsongpol, T.; Sirisinudomkit, P.; Pettong, T.; Sawangphruk, M. High-performance supercapacitor of functionalized carbon fiber paper with high surface ionic and bulk electronic conductivity: Effect of organic functional groups. *Electrochim. Acta* **2015**, *176*, 504–513. [CrossRef]
2. Sahoo, S.; Ratha, S.; Rout, C.S. Spinel $NiCo_2O_4$ nanorods for supercapacitor applications. *Am. J. Eng. Appl. Sci.* **2015**, *8*, 371–379. [CrossRef]

3. El-Kady, M.F.; Strong, V.; Dubin, S.; Kaner, R.B. Laser scribing of high-performance and flexible graphene-based electrochemical capacitors. *Science* **2012**, *335*, 1326–1330. [CrossRef]

4. Zhu, Y.; Murali, S.; Stoller, M.D.; Ganesh, K.J.; Cai, W.; Ferreira, P.J.; Pirkle, A.; Wallace, R.M.; Cychosz, K.A.; Thommes, M.; et al. Carbon-based supercapacitors produced by activation of graphene. *Science* **2011**, *332*, 1537–1541. [CrossRef]

5. Pettong, T.; Iamprasertkun, P.; Krittayavathananon, A.; Sukha, P.; Sirisinudomkit, P.; Seubsai, A.; Chareonpanich, M.; Kongkachuichay, P.; Limtrakul, J.; Sawangphruk, M. High-performance asymmetric supercapacitors of $MnCo_2O_4$ nanofibers and N-doped reduced graphene oxide aerogel. *ACS Appl. Mater. Interfaces* **2016**, *8*, 34045–34053. [CrossRef] [PubMed]

6. Fan, L.Z.; Qiao, S.; Song, W.; Wu, M.; He, X.; Qu, X. Effects of the functional groups on the electrochemical properties of ordered porous carbon for supercapacitors. *Electrochim. Acta* **2013**, *105*, 299–304. [CrossRef]

7. Chen, X.L.; Li, W.S.; Tan, C.L.; Li, W.; Wu, Y.Z. Improvement in electrochemical capacitance of carbon materials by nitric acid treatment. *J. Power Sources* **2008**, *184*, 668–674. [CrossRef]

8. Yang, Q.; Lu, Z.; Li, T.; Sun, X.; Liu, J. Hierarchical construction of core–shell metal oxide nanoarrays with ultrahigh areal capacitance. *Nano Energy* **2014**, *7*, 170–178. [CrossRef]

9. Vilatela, J.J.; Eder, D. Nanocarbon composites and hybrids in sustainability: A review. *ChemSusChem* **2012**, *5*, 456–478. [CrossRef]

10. Nguyen, T.; Montemor, M.D.F. Metal Oxide and Hydroxide–Based Aqueous Supercapacitors: From Charge Storage Mechanisms and Functional Electrode Engineering to Need-Tailored Devices. *Adv. Sci.* **2019**, *6*, 1801797. [CrossRef]

11. Alqahtani, D.M.; Zequine, C.; Ranaweera, C.K.; Siam, K.; Kahol, P.K.; Poudel, T.P.; Mishra, S.R.; Gupta, R.K. Effect of metal ion substitution on electrochemical properties of cobalt oxide. *J. Alloy. Compd.* **2019**, *771*, 951–959. [CrossRef]

12. Pendashteh, A.; Moosavifard, S.E.; Rahmanifar, M.S.; Wang, Y.; El-Kady, M.F.; Kaner, R.B.; Mousavi, M.F. Highly ordered mesoporous $CuCo_2O_4$ nanowires, a promising solution for high-performance supercapacitors. *Chem. Mater.* **2015**, *27*, 3919–3926. [CrossRef]

13. Cheng, H.; Lu, Z.G.; Deng, J.Q.; Chung, C.Y.; Zhang, K.; Li, Y.Y. A facile method to improve the high rate capability of Co_3O_4 nanowire array electrodes. *Nano Res.* **2010**, *3*, 895–901. [CrossRef]

14. Yan, D.; Zhang, H.; Chen, L.; Zhu, G.; Li, S.; Xu, H.; Yu, A. Biomorphic synthesis of mesoporous Co_3O_4 microtubules and their pseudocapacitive performance. *ACS Appl. Mater. Interfaces* **2014**, *6*, 15632–15637. [CrossRef] [PubMed]

15. Sieber, H. Biomimetic synthesis of ceramics and ceramic composites. *Mater. Sci. Eng. A* **2005**, *412*, 43–47. [CrossRef]

16. Habibi, Y.; Lucia, L.A.; Rojas, O.J. Cellulose nanocrystals: Chemistry, self-assembly, and applications. *Chem. Rev.* **2010**, *110*, 3479–3500. [CrossRef]

17. Liu, Y.; Lv, B.; Li, P.; Chen, Y.; Gao, B.; Lin, B. Biotemplate-assisted hydrothermal synthesis of tubular porous Co_3O_4 with excellent charge-discharge cycle stability for supercapacitive electrodes. *Mater. Lett.* **2018**, *210*, 231–234. [CrossRef]

18. Fan, T.X.; Chow, S.K.; Zhang, D. Biomorphic mineralization: From biology to materials. *Prog. Mater. Sci.* **2009**, *54*, 542–659. [CrossRef]

19. Sotiropoulou, S.; Sierra-Sastre, Y.; Mark, S.S.; Batt, C.A. Biotemplated nanostructured materials. *Chem. Mater.* **2008**, *20*, 821–834. [CrossRef]

20. Zhou, H.; Fan, T.; Zhang, D. Biotemplated materials for sustainable energy and environment: Current status and challenges. *ChemSusChem* **2011**, *4*, 1344–1387. [CrossRef]

21. Shim, H.W.; Lim, A.H.; Kim, J.C.; Jang, E.; Seo, S.D.; Lee, G.H.; Kim, T.D.; Kim, D.W. Scalable one-pot bacteria-templating synthesis route toward hierarchical, porous-Co_3O_4 superstructures for supercapacitor electrodes. *Sci. Rep.* **2013**, *3*, 2325. [CrossRef] [PubMed]

22. Han, L.; Yang, D.P.; Liu, A. Leaf-templated synthesis of 3D hierarchical porous cobalt oxide nanostructure as direct electrochemical biosensing interface with enhanced electrocatalysis. *Biosens. Bioelectron.* **2015**, *63*, 145–152. [CrossRef]

23. Song, P.; Zhang, H.; Han, D.; Li, J.; Yang, Z.; Wang, Q. Preparation of biomorphic porous $LaFeO_3$ by sorghum straw biotemplate method and its acetone sensing properties. *Sens. Actuators B Chem.* **2014**, *196*, 140–146. [CrossRef]

24. Weatherspoon, M.R.; Cai, Y.; Crne, M.; Srinivasarao, M.; Sandhage, K.H. 3D Rutile Titania-Based Structures with Morpho Butterfly Wing Scale Morphologies. *Angew. Chem. Int. Ed.* **2008**, *47*, 7921–7923. [CrossRef] [PubMed]

25. Yan, D.; Li, S.; Zhu, G.; Wang, Z.; Xu, H.; Yu, A. Synthesis and pseudocapacitive behaviors of biomorphic mesoporous tubular MnO_2 templated from cotton. *Mater. Lett.* **2013**, *95*, 164–167. [CrossRef]

26. Mondal, A.K.; Su, D.; Chen, S.; Ung, A.; Kim, H.S.; Wang, G. Mesoporous $MnCo_2O_4$ with a flake-like structure as advanced electrode materials for lithium-ion batteries and supercapacitors. *Chem. A Eur. J.* **2015**, *21*, 1526–1532. [CrossRef]

27. Xu, J.; Sun, Y.; Lu, M.; Wang, L.; Zhang, J.; Tao, E.; Qian, J.; Liu, X. Fabrication of the porous $MnCo_2O_4$ nanorod arrays on Ni foam as an advanced electrode for asymmetric supercapacitors. *Acta Mater.* **2018**, *152*, 162–174. [CrossRef]

28. Dong, Y.; Wang, Y.; Xu, Y.; Chen, C.; Wang, Y.; Jiao, L.; Yuan, H. Facile synthesis of hierarchical nanocage $MnCo_2O_4$ for high performance supercapacitor. *Electrochim. Acta* **2017**, *225*, 39–46. [CrossRef]

29. Yang, J.; Cho, M.; Lee, Y. Synthesis of hierarchical $NiCo_2O_4$ hollow nanorods via sacrificial-template accelerate hydrolysis for electrochemical glucose oxidation. *Biosens. Bioelectron.* **2016**, *75*, 15–22. [CrossRef]

30. Zhao, Z.; Geng, F.; Bai, J.; Cheng, H.M. Facile and controlled synthesis of 3D nanorods-based urchinlike and nanosheets-based flowerlike cobalt basic salt nanostructures. *J. Phys. Chem. C* **2007**, *111*, 3848–3852. [CrossRef]

31. Jadhav, A.R.; Bandal, H.A.; Kim, H. $NiCo_2O_4$ hollow sphere as an efficient catalyst for hydrogen generation by NaBH4 hydrolysis. *Mater. Lett.* **2017**, *198*, 50–53. [CrossRef]

32. Huang, W.; Lin, T.; Cao, Y.; Lai, X.; Peng, J.; Tu, J. Hierarchical $NiCo_2O_4$ hollow sphere as a peroxidase mimetic for colorimetric detection of H_2O_2 and glucose. *Sensors* **2017**, *17*, 217. [CrossRef]

33. Pu, J.; Wang, J.; Jin, X.; Cui, F.; Sheng, E.; Wang, Z. Porous hexagonal $NiCo_2O_4$ nanoplates as electrode materials for supercapacitors. *Electrochim. Acta* **2013**, *106*, 226–234. [CrossRef]

34. Park, J.; Shen, X.; Wang, G. Solvothermal synthesis and gas-sensing performance of Co_3O_4 hollow nanospheres. *Sens. Actuators B Chem.* **2009**, *136*, 494–498. [CrossRef]

35. Lasheras, X.; Insausti, M.; Gil de Muro, I.; Garaio, E.; Plazaola, F.; Moros, M.; De Matteis, L.; M de la Fuente, J.; Lezama, L. Chemical synthesis and magnetic properties of monodisperse nickel ferrite nanoparticles for biomedical applications. *J. Phys. Chem. C* **2016**, *120*, 3492–3500. [CrossRef]

36. Kuang, L.; Ji, F.; Pan, X.; Wang, D.; Chen, X.; Jiang, D.; Zhang, Y.; Ding, B. Mesoporous $MnCo_2O_4$ nanoneedle arrays electrode for high-performance asymmetric supercapacitor application. *Chem. Eng. J.* **2017**, *315*, 491–499. [CrossRef]

37. Melot, B.C.; Tarascon, J.M. Design and preparation of materials for advanced electrochemical storage. *Acc. Chem. Res.* **2013**, *46*, 1226–1238. [CrossRef]

38. Chen, K.; Xue, D. Materials chemistry toward electrochemical energy storage. *J. Mater. Chem. A* **2016**, *4*, 7522–7537. [CrossRef]

39. *Principles and Applications of Lithium Secondary Batteries*; Park, J.K. (Ed.) John Wiley & Sons: Hoboken, NJ, USA, 2012.

40. Zhang, Y.; Ma, M.; Yang, J.; Su, H.; Huang, W.; Dong, X. Selective synthesis of hierarchical mesoporous spinel $NiCo_2O_4$ for high-performance supercapacitors. *Nanoscale* **2014**, *6*, 4303–4308. [CrossRef]

41. Yuan, C.; Wu, H.B.; Xie, Y.; Lou, X.W. Mixed transition-metal oxides: Design, synthesis, and energy-related applications. *Angew. Chem. Int. Ed.* **2014**, *53*, 1488–1504. [CrossRef]

42. Zhang, L.L.; Zhao, X.S. Carbon-based materials as supercapacitor electrodes. *Chem. Soc. Rev.* **2009**, *38*, 2520–2531. [CrossRef]

43. Zheng, Y.Z.; Ding, H.; Uchaker, E.; Tao, X.; Chen, J.F.; Zhang, Q.; Cao, G. Nickel-mediated polyol synthesis of hierarchical V_2O_5 hollow microspheres with enhanced lithium storage properties. *J. Mater. Chem. A* **2015**, *3*, 1979–1985. [CrossRef]

44. *Lithium Batteries: Science and Technology*; Nazri, G.A.; Pistoia, G. (Eds.) Springer Science & Business Media: Berlin/Heidelberg, Germany, 2008.

45. Li, J.; Wang, J.; Liang, X.; Zhang, Z.; Liu, H.; Qian, Y.; Xiong, S. Hollow $MnCo_2O_4$ submicrospheres with multilevel interiors: From mesoporous spheres to yolk-in-double-shell structures. *ACS Appl. Mater. Interfaces* **2013**, *6*, 24–30. [CrossRef] [PubMed]

46. Bhojane, P.; Sen, S.; Shirage, P.M. Enhanced electrochemical performance of mesoporous NiCo$_2$O$_4$ as an excellent supercapacitive alternative energy storage material. *Appl. Surf. Sci.* **2016**, *377*, 376–384. [CrossRef]

47. Jenkins, R.; Snyder, R.L. *Introduction to X-ray Powder Diffractometry*; (No. 543.427 JEN); Wiley: Hoboken, NJ, USA, 1996.

48. Lin, H.K.; Chiu, H.C.; Tsai, H.C.; Chien, S.H.; Wang, C.B. Synthesis, characterization and catalytic oxidation of carbon monoxide over cobalt oxide. *Catal. Lett.* **2003**, *88*, 169–174. [CrossRef]

49. Spencer, C.D.; Schroeer, D. Mössbauer study of several cobalt spinels using Co^{57} and Fe^{57}. *Phys. Rev. B* **1974**, *9*, 3658. [CrossRef]

50. Kurtulus, F.; Guler, H. A Simple Microwave-Assisted Route to Prepare Black Cobalt, Co$_3$O$_4$. *Inorg. Mater.* **2005**, *41*, 483–485. [CrossRef]

51. St, G.C.; Stoyanova, M.; Georgieva, M.; Mehandjiev, D. Preparation and characterization of a higher cobalt oxide. *Mater. Chem. Phys.* **1999**, *60*, 39–43.

52. Khairy, M.; Mousa, M. Synthesis of Ternary and Quaternary metal oxides based on Ni, Mn, Cu, and Co for high-performance Supercapacitor. *J. Ovonic Res.* **2019**, *15*, 181–198.

53. Štěpánek, F.; Marek, M.; Adler, P.M. Modeling capillary condensation hysteresis cycles in reconstructed porous media. *Aiche J.* **1999**, *45*, 1901–1912. [CrossRef]

54. Wang, R.; Li, Q.; Cheng, L.; Li, H.; Wang, B.; Zhao, X.S.; Guo, P. Electrochemical properties of manganese ferrite-based supercapacitors in aqueous electrolyte: The effect of ionic radius. *Colloid. Surfaces A Physicochem. Eng. Aspects* **2014**, *457*, 94–99. [CrossRef]

55. Hou, L.; Yuan, C.; Yang, L.; Shen, L.; Zhang, F.; Zhang, X. Urchin-like Co$_3$O$_4$ microspherical hierarchical superstructures constructed by one-dimension nanowires toward electrochemical capacitors. *Rsc Adv.* **2011**, *1*, 1521–1526. [CrossRef]

56. Yuan, C.; Yang, L.; Hou, L.; Shen, L.; Zhang, X.; Lou, X.W.D. Growth of ultrathin mesoporous Co$_3$O$_4$ nanosheet arrays on Ni foam for high-performance electrochemical capacitors. *Energy Environ. Sci.* **2012**, *5*, 7883–7887. [CrossRef]

57. Adhikari, H.; Ghimire, M.; Ranaweera, C.K.; Bhoyate, S.; Gupta, R.K.; Alam, J.; Mishra, S.R. Synthesis and electrochemical performance of hydrothermally synthesized Co$_3$O$_4$ nanostructured particles in presence of urea. *J. Alloy. Compd.* **2017**, *708*, 628–638. [CrossRef]

58. Sun, D.; He, L.; Chen, R.; Liu, Y.; Lv, B.; Lin, S.; Lin, B. Biomorphic composites composed of octahedral Co3O4 nanocrystals and mesoporous carbon microtubes templated from cotton for excellent supercapacitor electrodes. *Appl. Surf. Sci.* **2019**, *465*, 232–240. [CrossRef]

59. Brousse, T.; Bélanger, D. A Hybrid Fe$_3$O$_4$ MnO$_2$ Capacitor in Mild Aqueous Electrolyte. *Electrochem. Solid-State Lett.* **2003**, *6*, A244–A248. [CrossRef]

60. Wang, S.Y.; Ho, K.C.; Kuo, S.L.; Wu, N.L. Investigation on capacitance mechanisms of Fe$_3$O$_4$ electrochemical capacitors. *J. Electrochem. Soc.* **2006**, *153*, A75–A80. [CrossRef]

61. Tiruye, G.A.; Munoz-Torrero, D.; Palma, J.; Anderson, M.; Marcilla, R. All-solid state supercapacitors operating at 3.5 V by using ionic liquid based polymer electrolytes. *J. Power Sources* **2015**, *279*, 472–480. [CrossRef]

62. Gao, F.; Shao, G.; Qu, J.; Lv, S.; Li, Y.; Wu, M. Tailoring of porous and nitrogen-rich carbons derived from hydrochar for high-performance supercapacitor electrodes. *Electrochim. Acta* **2015**, *155*, 201–208. [CrossRef]

63. Selvam, M.; Srither, S.R.; Saminathan, K.; Rajendran, V. Chemically and electrochemically prepared graphene/MnO$_2$ nanocomposite electrodes for zinc primary cells: A comparative study. *Ionics* **2015**, *21*, 791–799. [CrossRef]

64. Tang, Y.; Liu, Y.; Yu, S.; Gao, F.; Zhao, Y. Comparative study on three commercial carbons for supercapacitor applications. *Russ. J. Electrochem.* **2015**, *51*, 77–85. [CrossRef]

65. Sankar, K.V.; Selvan, R.K. Improved electrochemical performances of reduced graphene oxide based supercapacitor using redox additive electrolyte. *Carbon* **2015**, *90*, 260–273. [CrossRef]

66. Sahu, V.; Shekhar, S.; Sharma, R.K.; Singh, G. Ultrahigh performance supercapacitor from lacey reduced graphene oxide nanoribbons. *ACS Appl. Mater. Interfaces* **2015**, *7*, 3110–3116. [CrossRef] [PubMed]

67. Fic, K.; Platek, A.; Piwek, J.; Frackowiak, E. Sustainable materials for electrochemical capacitors. *Mater. Today* **2018**, *21*, 437–454. [CrossRef]

68. Meher, S.K.; Justin, P.; Rao, G.R. Nanoscale morphology dependent pseudocapacitance of NiO: Influence of intercalating anions during synthesis. *Nanoscale* **2011**, *3*, 683–692. [CrossRef]

69. Xiao, J.; Yang, S. Sequential crystallization of sea urchin-like bimetallic (Ni, Co) carbonate hydroxide and its morphology conserved conversion to porous NiCo$_2$O$_4$ spinel for pseudocapacitors. *Rsc Adv.* **2011**, *1*, 588–595. [CrossRef]

70. Liu, X.Y.; Zhang, Y.Q.; Xia, X.H.; Shi, S.J.; Lu, Y.; Wang, X.L.; Gu, C.D.; Tu, J.P. Self-assembled porous NiCo$_2$O$_4$ hetero-structure array for electrochemical capacitor. *J. Power Sources* **2013**, *239*, 157–163. [CrossRef]

71. Wang, X.; Han, X.; Lim, M.; Singh, N.; Gan, C.L.; Jan, M.; Lee, P.S. Nickel cobalt oxide-single wall carbon nanotube composite material for superior cycling stability and high-performance supercapacitor application. *J. Phys. Chem. C* **2012**, *116*, 12448–12454. [CrossRef]

72. Liu, X.; Long, Q.; Jiang, C.; Zhan, B.; Li, C.; Liu, S.; Zhao, Q.; Huang, W.; Dong, X. Facile and green synthesis of mesoporous Co$_3$O$_4$ nanocubes and their applications for supercapacitors. *Nanoscale* **2013**, *5*, 6525–6529. [CrossRef]

73. Zhu, Y.; Pu, X.; Song, W.; Wu, Z.; Zhou, Z.; He, X.; Lu, F.; Jing, M.; Tang, B.; Ji, X. High capacity NiCo$_2$O$_4$ nanorods as electrode materials for supercapacitor. *J. Alloy. Compd.* **2014**, *617*, 988–993. [CrossRef]

74. Jokar, E.; Shahrokhian, S. Synthesis and characterization of NiCo$_2$O$_4$ nanorods for preparation of supercapacitor electrodes. *J. Solid State Electrochem.* **2015**, *19*, 269–274. [CrossRef]

75. Veeramani, V.; Madhu, R.; Chen, S.M.; Sivakumar, M.; Hung, C.T.; Miyamoto, N.; Liu, S.B. NiCo$_2$O$_4$-decorated porous carbon nanosheets for high-performance supercapacitors. *Electrochim. Acta* **2017**, *247*, 288–295. [CrossRef]

76. Zhai, Y.; Mao, H.; Liu, P.; Ren, X.; Xu, L.; Qian, Y. Facile fabrication of hierarchical porous rose-like NiCo$_2$O$_4$ nanoflake/MnCo$_2$O$_4$ nanoparticle composites with enhanced electrochemical performance for energy storage. *J. Mater. Chem. A* **2015**, *3*, 16142–16149. [CrossRef]

77. Ghosh, D.; Giri, S.; Das, C.K. Hydrothermal synthesis of platelet β Co(OH)$_2$ and Co$_3$O$_4$: Smart electrode material for energy storage application. *Environ. Prog. Sustain. Energy* **2014**, *33*, 1059–1064. [CrossRef]

78. Yi, H.; Wang, H.; Jing, Y.; Peng, T.; Wang, X. Asymmetric supercapacitors based on carbon nanotubes@ NiO ultrathin nanosheets core-shell composites and MOF-derived porous carbon polyhedrons with super-long cycle life. *J. Power Sources* **2015**, *285*, 281–290. [CrossRef]

79. Shen, B.; Guo, R.; Lang, J.; Liu, L.; Liu, L.; Yan, X. A high-temperature flexible supercapacitor based on pseudocapacitive behavior of FeOOH in an ionic liquid electrolyte. *J. Mater. Chem. A* **2016**, *4*, 8316–8327. [CrossRef]

80. Augustyn, V.; Come, J.; Lowe, M.A.; Kim, J.W.; Taberna, P.L.; Tolbert, S.H.; Abruña, H.D.; Simon, P.; Dunn, B. High-rate electrochemical energy storage through Li$^+$ intercalation pseudocapacitance. *Nat. Mater.* **2013**, *12*, 518. [CrossRef]

81. Lindström, H.; Södergren, S.; Solbrand, A.; Rensmo, H.; Hjelm, J.; Hagfeldt, A.; Lindquist, S.E. Li$^+$ ion insertion in TiO$_2$ (anatase). 1. Chronoamperometry on CVD films and nanoporous films. *J. Phys. Chem. B* **1997**, *101*, 7710–7716. [CrossRef]

82. Liu, T.C.; Pell, W.G.; Conway, B.E.; Roberson, S.L. Behavior of molybdenum nitrides as materials for electrochemical capacitors comparison with ruthenium oxide. *J. Electrochem. Soc.* **1998**, *145*, 1882–1888. [CrossRef]

83. Wang, J.; Polleux, J.; Lim, J.; Dunn, B. Pseudocapacitive contributions to electrochemical energy storage in TiO$_2$ (anatase) nanoparticles. *J. Phys. Chem. C* **2007**, *111*, 14925–14931. [CrossRef]

84. Zhao, D.D.; Bao, S.J.; Zhou, W.J.; Li, H.L. Preparation of hexagonal nanoporous nickel hydroxide film and its application for electrochemical capacitor. *Electrochem. Commun.* **2007**, *9*, 869–874. [CrossRef]

85. Sugimoto, W.; Iwata, H.; Yasunaga, Y.; Murakami, Y.; Takasu, Y. Preparation of ruthenic acid nanosheets and utilization of its interlayer surface for electrochemical energy storage. *Angew. Chem. Int. Ed.* **2003**, *42*, 4092–4096. [CrossRef] [PubMed]

86. Li, L.; Zhang, Y.Q.; Liu, X.Y.; Shi, S.J.; Zhao, X.Y.; Zhang, H.; Ge, X.; Cai, G.F.; Gu, C.D.; Wang, X.L.; et al. One-dimension MnCo$_2$O$_4$ nanowire arrays for electrochemical energy storage. *Electrochim. Acta* **2014**, *116*, 467–474. [CrossRef]

87. Hui, K.N.; San Hui, K.; Tang, Z.; Jadhav, V.V.; Xia, Q.X. Hierarchical chestnut-like MnCo$_2$O$_4$ nanoneedles grown on nickel foam as binder-free electrode for high energy density asymmetric supercapacitors. *J. Power Sources* **2016**, *330*, 195–203. [CrossRef]

88. Shi, X.; Liu, Z.; Zheng, Y.; Zhou, G. Controllable synthesis and electrochemical properties of MnCo$_2$O$_4$ nanorods and microcubes. *Colloids Surf. A: Physicochem. Eng. Asp.* **2017**, *522*, 525–535. [CrossRef]

89. Liu, S.; Hui, K.S.; Hui, K.N. 1 D hierarchical MnCo$_2$O$_4$ nanowire@ MnO$_2$ sheet core–shell arrays on graphite paper as superior electrodes for asymmetric supercapacitors. *ChemNanoMat* **2015**, *1*, 593–602. [CrossRef]

90. Venkatachalam, V.; Alsalme, A.; Alghamdi, A.; Jayavel, R. High performance electrochemical capacitor based on MnCo$_2$O$_4$ nanostructured electrode. *J. Electroanal. Chem.* **2015**, *756*, 94–100. [CrossRef]

91. Zhu, Y.; Ji, X.; Yin, R.; Hu, Z.; Qiu, X.; Wu, Z.; Liu, Y. Nanorod-assembled NiCo$_2$O$_4$ hollow microspheres assisted by an ionic liquid as advanced electrode materials for supercapacitors. *Rsc Adv.* **2017**, *7*, 11123–11128. [CrossRef]

92. Mao, J.W.; He, C.H.; Qi, J.Q.; Zhang, A.B.; Sui, Y.W.; He, Y.Z.; Meng, Q.K.; Wei, F.X. An Asymmetric Supercapacitor with Mesoporous NiCo$_2$O$_4$ Nanorod/Graphene Composite and N-Doped Graphene Electrodes. *J. Electron. Mater.* **2018**, *47*, 512–520. [CrossRef]

93. Jabeen, N.; Xia, Q.; Yang, M.; Xia, H. Unique core–shell nanorod arrays with polyaniline deposited into mesoporous NiCo$_2$O$_4$ support for high-performance supercapacitor electrodes. *Acs Appl. Mater. Interfaces* **2016**, *8*, 6093–6100. [CrossRef]

94. Srinivasan, V.; Weidner, J.W. Studies on the capacitance of nickel oxide films: Effect of heating temperature and electrolyte concentration. *J. Electrochem. Soc.* **2000**, *147*, 880–885. [CrossRef]

95. Lin, C.; Ritter, J.A.; Popov, B.N. Characterization of sol-gel-derived cobalt oxide xerogels as electrochemical capacitors. *J. Electrochem. Soc.* **1998**, *145*, 4097–4103. [CrossRef]

96. Zhi, M.; Xiang, C.; Li, J.; Li, M.; Wu, N. Nanostructured carbon–metal oxide composite electrodes for supercapacitors: A review. *Nanoscale* **2013**, *5*, 72–88. [CrossRef] [PubMed]

97. Wu, Z.; Zhu, Y.; Ji, X. NiCo$_2$O$_4$-based materials for electrochemical supercapacitors. *J. Mater. Chem. A* **2014**, *2*, 14759–14772. [CrossRef]

98. Bitla, Y.; Chin, Y.Y.; Lin, J.C.; Van, C.N.; Liu, R.; Zhu, Y.; Liu, H.J.; Zhan, Q.; Lin, H.J.; Chen, C.T.; et al. Origin of metallic behavior in NiCo 2 O 4 ferrimagnet. *Sci. Rep.* **2015**, *5*, 15201. [CrossRef]